

Ultrarelativistic fluid dynamics

David W Neilsen[†] and Matthew W Choptuik^{†‡}

[†] Center for Relativity, The University of Texas at Austin, Austin, TX 78712-1081, USA

[‡] Department of Physics & Astronomy, University of British Columbia, Vancouver BC, Canada V6T 1Z1

Received 19 April 1999

Abstract. This is the first of two papers examining the critical collapse of spherically symmetric perfect fluids with the equation of state $P = (\Gamma - 1)\rho$. Here we present the equations of motion and describe a computer code capable of simulating the extremely relativistic flows encountered in critical solutions for $\Gamma \leq 2$. The fluid equations are solved using a high-resolution shock-capturing scheme based on a linearized Riemann solver.

PACS numbers: 0420D, 0425D, 0440N, 0470B, 0260, 0260C

1. Introduction

This paper describes a new computer code for simulating a self-gravitating, relativistic perfect fluid in spherical symmetry, with the equation of state

$$P = (\Gamma - 1)\rho. \quad (1)$$

Here, P and ρ are the fluid pressure and total energy density, respectively, and Γ is a constant satisfying $1 < \Gamma \leq 2$. The code has been optimized for *ultrarelativistic* fluid flows with Lorentz factors much larger than unity. This optimization involves a novel definition of the fluid variables, the use of a modern high-resolution shock-capturing scheme and care in reconstruction of the primitive fluid variables (the pressure and velocity) from the conserved quantities actually evolved by the code.

Our new code was specifically developed to study the critical gravitational collapse of perfect fluids, especially in the limit $\Gamma \rightarrow 2$. Critical collapse has become an interesting subfield in general relativity since its initial discovery in the massless Klein–Gordon system [1], and the perfect-fluid model has played an important role in advancing our understanding of the critical phenomena which arise at the threshold of black-hole formation. (For an excellent introduction to critical phenomena, see the review by Gundlach [2].) While the critical solutions for perfect fluids in spherical symmetry have been the subject of recent study [3–11], the precise nature of the critical solutions for $\Gamma \gtrsim 1.89$ was not previously known, and thus one of the chief goals of our investigation was a thorough analysis of this regime. In the remainder of this paper we describe the equations of motion which are solved, and the numerical techniques which we use to solve them. A companion paper [12] describes in detail the results we have generated with the code.

2. Geometry and fluid model

The Einstein equations couple the spacetime geometry, encoded in the Einstein tensor, G_{ab} , to the stress–energy tensor, T_{ab} , of the spacetime’s matter/fields

$$G_{ab} = 8\pi T_{ab}, \quad (2)$$

(here and throughout, we use units in which the speed of light and Newton’s gravitation constant are unity: $c = 1$ and $G = 1$, and Latin indices a, b, c, \dots take on the spacetime values 0, 1, 2, 3). A fluid is a continuum model for a large number of particles that uses the macroscopic properties of a thermodynamic system, such as the internal energy and pressure, as fundamental dynamical variables. A perfect fluid has neither shear stresses nor dissipative forces, and has a stress–energy tensor

$$T_{ab} = (\rho + P)u_a u_b + P g_{ab}, \quad (3)$$

where ρ is the energy density, P is the pressure, u_a is the fluid’s 4-velocity and g_{ab} is the spacetime metric. The energy density ρ contains *all* contributions to the total energy, which for a perfect fluid include the rest mass–energy density, ρ_0 , and the internal energy density

$$\rho = \rho_0 + \rho_0 \epsilon, \quad (4)$$

where ϵ is the specific internal energy. We consider only single-component fluids, and the number density, n , is simply related to ρ_0 via

$$\rho_0 = mn, \quad (5)$$

where m is the rest mass of a single fluid particle. The basic equations of motion for the fluid can be derived from local conservation of (a) the energy–momentum

$$\nabla_a T^{ab} = 0, \quad (6)$$

and (b) the particle number

$$\nabla_a (n u^a) = 0, \quad (7)$$

where ∇_a is the (covariant) derivative operator compatible with g_{ab} . To these conservation laws one must adjoin an equation of state, $P = P(\rho_0, \epsilon)$, which, further, must be consistent with the first law of thermodynamics.

2.1. Equation of state

The equation of state (EOS) closes the fluid equations by providing a relationship between the pressure and (in our case) the rest energy density and internal energy. The nature of this relationship provides much of the physics for a given system. As mentioned in the introduction, our primary motivation for exploring ultrarelativistic fluid dynamics is to study perfect-fluid critical solutions. We expect these solutions to be scale invariant (self-similar), and we therefore choose an EOS compatible with this symmetry. The EOS

$$P = (\Gamma - 1)\rho, \quad (8)$$

where Γ is a constant, is the *only* EOS of the form $P = P(\rho)$ which is compatible with self-similarity [13–15], and is notable for the fact that it results in a sound speed, c_s , which is independent of density:

$$c_s = \sqrt{\frac{dP}{d\rho}} = \sqrt{\Gamma - 1}. \quad (9)$$

One can argue that this EOS is particularly appropriate for ultrarelativistic fluids, and hence we will refer to (8) as the *ultrarelativistic equation of state*. We note that the EOS for a ‘radiation fluid’ corresponds to $\Gamma = \frac{4}{3}$, while $\Gamma = 1$ gives a pressureless fluid (dust). We do not consider the case of dust collapse here; hence, in what follows, $1 < \Gamma \leq 2$.

The relativistic ideal gas is another important fluid model, with the equation of state

$$P = (\Gamma - 1)\rho_0\epsilon. \tag{10}$$

In the ultrarelativistic limit, the kinetic energy, $\rho_0\epsilon$, of the constituent particles of the fluid (or internal energy of the fluid in a thermodynamic context) is much larger than the mass–energy, ρ_0 , so we have $\rho \approx \rho_0\epsilon$. Thus, we interpret the EOS (8) as the ultrarelativistic limit of the ideal-gas EOS. As discussed in [12], the ultrarelativistic ideal gas becomes, in a limiting sense, scale invariant. As the critical solutions reside in this ultrarelativistic limit, we expect the critical solutions for fluids with the ideal-gas EOS to be identical to the critical solutions computed using (8). For this reason, hereafter we limit our attention to the ultrarelativistic equation of state.

2.2. Geometric equations of motion

We use the Arnowit–Deser–Misner (ADM) 3+1 formalism (specialized to spherical symmetry) to integrate the Einstein equations, and choose polar–areal coordinates for simplicity of the equations of motion, and for singularity avoidance. Specifically, adopting a polar–spherical coordinate system (t, r, θ, ϕ) , we write the spacetime metric as

$$ds^2 = -\alpha(r, t)^2 dt^2 + a(r, t)^2 dr^2 + r^2 (d\theta^2 + \sin^2 \theta d\phi^2), \tag{11}$$

wherein the radial coordinate, r , directly measures proper surface area. In analogy with the usual Schwarzschild form of the static spherically symmetric metric, it is also useful to define the mass aspect function

$$m(r, t) \equiv \frac{r}{2} \left(1 - \frac{1}{a^2} \right). \tag{12}$$

The fluid’s coordinate velocity, v , and the associated Lorentz gamma function, W , are defined by

$$v(r, t) \equiv \frac{au^r}{\alpha u^t}, \quad W(r, t) \equiv \alpha u^t. \tag{13}$$

Since the fluid 4-velocity is a unit-length, timelike vector ($u^a u_a = -1$), we then have the usual relation between W and v :

$$W^2 = \frac{1}{1 - v^2}. \tag{14}$$

We now introduce two *conservative* variables

$$\begin{aligned} \tau(r, t) &\equiv (\rho + P)W^2 - P \\ S(r, t) &\equiv (\rho + P)W^2 v, \end{aligned} \tag{15}$$

so named because they allow the fluid equations of motion to be written in *conservative form* (albeit with the addition of a source term), as discussed in detail in section 3.1. In contrast to the conservative variables, we refer to the pressure and velocity as *primitive* variables. With the above definitions, the non-zero components of the stress–energy tensor are

$$\begin{aligned} T^t_t &= -\tau & T^r_r &= Sv + P \\ T^t_r &= \frac{a}{\alpha} S & T^\theta_\theta &= T^\phi_\phi = P. \end{aligned} \tag{16}$$

A sufficient set of Einstein equations for the geometric variables a and α are given by (a) the non-trivial component of the momentum constraint (the notation $\partial_x f$ denotes partial differentiation, i.e. $\partial_x f \equiv \partial f / \partial x$)

$$\partial_t a = -4\pi r \alpha a^2 S, \quad (17)$$

and by (b) the polar slicing condition, which follows from the demand that metric should have the form (11) for all t :

$$\partial_r (\ln \alpha) = a^2 \left[4\pi r (Sv + P) + \frac{m}{r^2} \right]. \quad (18)$$

An additional equation for $a(r, t)$,

$$\partial_r a = a^3 \left(4\pi r \tau - \frac{m}{r^2} \right), \quad (19)$$

follows from the Hamiltonian constraint.

2.3. Fluid equations of motion

Because the equation of state is *not* a function of the number density, the time evolution of an ultrarelativistic perfect fluid is completely determined by conservation of the stress–energy tensor, i.e. from $\nabla_a T^{ab} = 0$. Given this fact, the derivation of the fluid equations of motion, which can naturally be written in conservative form, is a straightforward piece of analysis, and will not be given in detail here. Instead, we will simply quote the results, and for convenience in discussing the numerical method of solution, we adopt a ‘state vector’ notation. We define two vectors, \hat{q} and w , which are the conservative and primitive variables, respectively,

$$\hat{q} \equiv \begin{bmatrix} \tau \\ S \end{bmatrix}, \quad w \equiv \begin{bmatrix} P \\ v \end{bmatrix}. \quad (20)$$

We then define a ‘flux vector,’ \hat{f} , and a ‘source vector,’ $\hat{\psi}$,

$$\hat{f} \equiv \begin{bmatrix} S \\ Sv + P \end{bmatrix}, \quad \hat{\psi} \equiv \begin{bmatrix} 0 \\ \Sigma \end{bmatrix}. \quad (21)$$

These variables have been introduced with a hat ($\hat{}$) to distinguish them from the new variables defined in section 2.4, which are subsequently used in the actual numerical solution algorithm. Further, to expedite the discretization of the equations of motion, we decompose the source term, Σ , into two pieces, as follows:

$$\Sigma \equiv \Theta + \frac{2\alpha P}{ar}, \quad (22)$$

where

$$\Theta \equiv (Sv - \tau) \left(8\pi \alpha ar P + \alpha a \frac{m}{r^2} \right) + \alpha a P \frac{m}{r^2}. \quad (23)$$

(The momentum and Hamiltonian constraints have been used to simplify these expressions.) We note that in spherically symmetric Minkowski spacetime we have $\Sigma = 2P/r$. With the above definitions, we can now write the fluid equations of motion in the conservative form

$$\partial_t \hat{q} + \frac{1}{r^2} \partial_r (r^2 X \hat{f}) = \hat{\psi}, \quad (24)$$

where

$$X \equiv \frac{\alpha}{a} \tag{25}$$

is a purely geometric quantity.

The fluid equations of motion (24) contain a mixture of conservative and primitive variables, and thus it is necessary to transform between both sets of variables at each step in the integration procedure. The primitive variables w can be expressed in terms of the conservative variables \hat{q} by inverting the definitions (15) of the conservative variables:

$$P = -2\beta\tau + [4\beta^2\tau^2 + (\Gamma - 1)(\tau^2 - S^2)]^{1/2} \tag{26}$$

$$v = \frac{S}{\tau + P}. \tag{27}$$

Here the non-negative constant β is defined by

$$\beta \equiv \frac{1}{4}(2 - \Gamma). \tag{28}$$

The pressure equation (26) follows from the solution of a quadratic with a specific root chosen to yield a physical (non-negative) pressure. This demand ($P \geq 0$) further requires that $\tau \geq |S|$. A second physical requirement is that v be bounded by the speed of light, $|v| < 1$, and from (27) this will clearly be automatically satisfied when $\tau > |S|$. These physical restrictions on the primitive variables can sometimes be violated in numerical solutions of the fluid equations, and we discuss some numerical techniques aimed at ameliorating such difficulties in sections 4.3 and 4.4. Finally, we note that the above transformation from \hat{q} to w is particularly simple, in that it can be expressed *algebraically*. The corresponding transformation for the ideal-gas EOS (10) involves a transcendental equation, which, in a numerical implementation, must be solved iteratively at each grid point.

2.4. New conservative fluid variables

Using the conservative variables, \hat{q} , defined above, and the numerical method described in sections 3 and 4, we developed a preliminary code to solve the relativistic fluid equations. We then tested this code in Minkowski spacetime using slab and spherical symmetry. The tests in slab symmetry were completely satisfactory, modulo the convergence limitations of the numerical scheme (see section 4.7). However, in spherical symmetry, we found that our method frequently failed for ‘stiffer’ fluids ($\Gamma \gtrsim 1.9$), most notably in ‘evacuation regions’ where $\rho \rightarrow 0$ and $|v| \rightarrow 1$, a combination difficult for numerical work. These problems in spherical symmetry led us to seek a new set of conservative variables, and to motivate this change of variables, first consider the evolutions shown in figure 1. Here we begin with a time-symmetric, spherical shell of fluid, which has a Gaussian energy density profile. Owing to the time symmetry, as the evolution unfolds, the shell naturally splits into two sub-shells—one in-going and one out-going—and as the sub-shells separate, a new evacuation region forms in the region where the fluid was originally concentrated. Examination of the conservative variable profiles reveals that $|S| \approx \tau$, and this observation suggests that we adopt new variables

$$\Phi \equiv \tau - S, \quad \Pi \equiv \tau + S, \tag{29}$$

which loosely represent the in-going (Φ) and out-going (Π) parts of the solution. Thus our new state vector of conservative variables is

$$q \equiv \begin{bmatrix} \Pi \\ \Phi \end{bmatrix}. \tag{30}$$

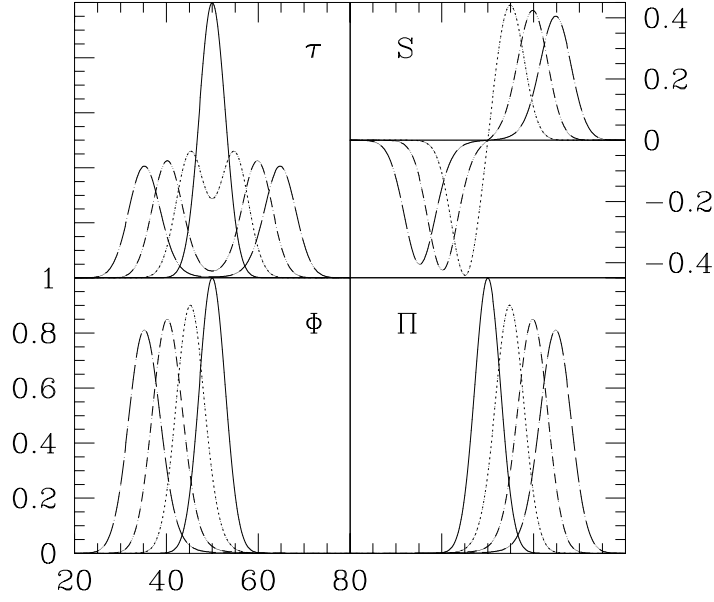


Figure 1. These plots show various fluid quantities at four different instances (equally spaced in time) in a flat spacetime, slab-symmetric evolution with $\Gamma = 1.9$. The initial configuration is a time-symmetric Gaussian pulse. The top frames show the evolution of the original conservative variables, τ and S . As the evolution proceeds, the pulse separates into left- and right-moving halves, and a vacuum region ($\tau \rightarrow 0$) develops between the two sub-pulses. The bottom frames show the evolution of the new conservative variables, Π and Φ , which do not divide into two shells as does τ . The correspondence of the new variables to left- and right-moving ‘waves’ is also evident. Note that the plots of τ , Π and Φ have the same vertical scale, while the vertical scale for S is shown separately. The horizontal scale is the same for all of the plots.

The \mathbf{q} variables provide a *significant* improvement over $\tilde{\mathbf{q}}$ in spherical symmetry with $\Gamma \gtrsim 1.9$. Not surprisingly, this change of variables does not solve *all* of the numerical problems encountered in the highly relativistic evacuation regions. For example, the new variables do not eliminate the need for a floor when searching for $\Gamma \gtrsim 1.9$ critical solutions.

The equations of motion for the new variables \mathbf{q} can be readily found by adding and subtracting the two components of (24), giving

$$\partial_t \mathbf{q} + \frac{1}{r^2} \partial_r [r^2 X \mathbf{f}] = \psi, \quad (31)$$

where the flux and source terms are now given by

$$\mathbf{f} \equiv \begin{bmatrix} \frac{1}{2}(\Pi - \Phi)(1 + v) + P \\ \frac{1}{2}(\Pi - \Phi)(1 - v) - P \end{bmatrix}, \quad \psi \equiv \begin{bmatrix} \Sigma \\ -\Sigma \end{bmatrix}. \quad (32)$$

The transformation from conservative to primitive variables can be found by simply changing variables in (26) and (27),

$$P = -\beta(\Pi + \Phi) + [\beta^2(\Pi + \Phi)^2 + (\Gamma - 1)\Pi\Phi]^{1/2}, \quad (33)$$

$$v = \frac{\Pi - \Phi}{\Pi + \Phi + 2P}. \quad (34)$$

Given the physical restriction $\tau > |S|$, the new variables \mathbf{q} are strictly positive: $\Pi > 0$, $\Phi > 0$.

2.5. The perfect fluid as a scalar field

There is a well known relation between an irrotational, stiff ($\Gamma = 2$) perfect fluid and a massless Klein–Gordon scalar field. In this section we discuss the relationship between scalar fields and perfect fluids for $1 < \Gamma \leq 2$. The perfect-fluid equations of motion

$$\nabla_a T^{ab} = 0, \quad (35)$$

can be written in terms of ρ , P , and u^a as

$$u^a \nabla_a \rho + (\rho + P) \nabla_a u^a = 0, \quad (36)$$

$$(\rho + P) u^a \nabla_a u^b + (g^{ab} + u^a u^b) \nabla_a P = 0. \quad (37)$$

If we assume the ultrarelativistic equation of state, $P = (\Gamma - 1)\rho$, then these equations become

$$\nabla_a (\rho^{1/\Gamma} u^a) = 0, \quad (38)$$

$$u^a \nabla_a u^b + \frac{(\Gamma - 1)}{\Gamma} (g^{ab} + u^a u^b) \nabla_a \ln \rho = 0, \quad (39)$$

provided that $\rho > 0$. We seek a specific combination of ρ and u^a that allows the fluid equations to be written in terms of a single variable, and therefore introduce the ansatz

$$w^a \equiv \rho^\mu u^a, \quad (40)$$

where μ is a constant that will be determined below. From elementary contractions we can express both ρ and u^a in terms of w^a

$$\rho = (-w_a w^a)^{1/2\mu}, \quad (41)$$

$$u^a = (-w_b w^b)^{-1/2} w^a. \quad (42)$$

However, it remains to be seen whether μ can be chosen such that w^a will satisfy the fluid equations of motion. We substitute expressions (41) and (42) into the momentum equation (37), and find that this equation is satisfied provided that

$$\mu = \frac{\Gamma - 1}{\Gamma}, \quad (43)$$

and

$$\nabla_{[a} w_{b]} = 0. \quad (44)$$

This latter condition allows one to write w^a as the gradient of a scalar field

$$w_a = \nabla_a \varphi. \quad (45)$$

The equation of motion for φ is obtained from (36)

$$\nabla_a [(-\nabla_c \varphi \nabla^c \varphi)^v \nabla^a \varphi] = 0, \quad (46)$$

where

$$v = \frac{2 - \Gamma}{2(\Gamma - 1)}. \quad (47)$$

The condition (44), $\nabla_{[a} w_{b]} = 0$, reduces to the requirement that the fluid be irrotational

$$\nabla_{[a} u_{b]} = 0. \quad (48)$$

Thus, the fluid equations for an ultrarelativistic, irrotational fluid can be written in terms of a nonlinear equation for a scalar field, φ . For the stiff fluid ($\Gamma = 2$), we find that the equation of motion for φ becomes the massless Klein–Gordon equation

$$\nabla_a \nabla^a \varphi = 0, \quad (\Gamma = 2). \quad (49)$$

One typically places physically motivated conditions on the fluid variables, such as $\rho > 0$ and $u^a u_a = -1$. Solutions of the Klein–Gordon equation, however, have timelike, null and spacelike gradients ($\nabla_a \varphi$). With the usual physical constraints on the fluid, then only a subset of possible Klein–Gordon solutions can be interpreted as $\Gamma = 2$ perfect fluids, namely those with $\nabla_a \varphi \nabla^a \varphi < 0$.

3. Numerical methods for fluid equations

An important consideration for numerical solutions of compressible fluid flow is how the numerical method will respond to the presence or formation of shocks, i.e. discontinuities in the fluid variables. These discontinuities often cause the dramatic failure of naive finite-difference schemes, and as shocks form *generically* from smooth initial data, many special techniques have been developed for numerically solving the fluid equations. One approach is to introduce an *artificial viscosity* that adds extra dissipation in the vicinity of a shock, spreading the would-be discontinuity over a few grid points. This technique has been widely used, and has the advantages of simplicity of implementation and computational efficiency. However, Norman and Winkler [16] investigated the use of artificial viscosity in relativistic flows, and showed that an *explicit* numerical scheme treats the artificial viscosity term inconsistently in relativistic fluid dynamics, leading to large numerical errors in the ultrarelativistic limit, $W \gg 1$. A second approach to solving the fluid equations with shocks comes from methods developed specifically for conservation laws. These methods, usually variations or extensions of Godunov’s original idea [17] to use a piecewise solution of the Riemann problem, have proven to be very reliable and robust. LeVeque [18, 19] has written excellent introductions to conservative methods, and our presentation here is in the spirit of his work. Furthermore, the application of these methods to problems in relativistic astrophysics has been recently reviewed by Ibáñez and Martí [20]. However, for the sake of completeness, we first briefly define and discuss conservation laws, and outline a general approach for their solution. We then discuss a linear Riemann solver and a cell reconstruction method that results in a scheme which, for smooth flows, is second-order accurate in the mesh spacing.

3.1. Conservation methods

Conservation laws greatly simplify the mathematical description of physical systems by focusing on quantities Q —where Q may be a state vector with multiple components—that do not change with time

$$\partial_t \int_V dQ = 0. \quad (50)$$

In this section we discuss the derivation of numerical schemes for this specific and important case where $\int dQ$ is conserved on the computational domain. Our discussion will be general, and not specifically tailored for the fluid partial differential equations (PDEs) derived in section 2.4, but for simplicity we restrict the discussion to one-dimensional (in space) systems.

While conservation laws are often written in *differential* form (e.g. $\nabla_a T^{ab} = 0$) it is useful to first consider an *integral* formulation, which is often the more fundamental expression.

Consider an arbitrary volume or cell, C_i , with a domain $[x_1, x_2]$. The quantity of \mathcal{Q} within C_i is denoted by \mathcal{Q}_i , and we define a density function q such that

$$\mathcal{Q}_i = \int_{x_1}^{x_2} dx q. \quad (51)$$

The change of \mathcal{Q}_i with time can be calculated from the flux, $f(q)$, of q through the cell boundaries. This consideration thus yields our conservation law:

$$\frac{d}{dt} \int_{x_1}^{x_2} dx q(x, t) = f(q(x_1, t)) - f(q(x_2, t)). \quad (52)$$

The conservation law can be written in *integral* form by integrating (52) from an initial time, t_1 , to a final time, t_2 ,

$$\int_{x_1}^{x_2} dx q(x, t_2) = \int_{x_1}^{x_2} dx q(x, t_1) + \int_{t_1}^{t_2} dt f(q(x_1, t)) - \int_{t_1}^{t_2} dt f(q(x_2, t)) \quad (53)$$

and the differential form follows from further manipulation *if* we assume that q is differentiable:

$$\partial_t q + \partial_x f(q) = 0. \quad (54)$$

It should be emphasized that the integral formulation should be viewed as *the* primary mathematical form for a conservation principle, because it is *not* dependent on an assumption of differentiability. For example, at a shock front in a fluid system, q is not differentiable, and the differential form of the conservation law fails, while the integral formulation is still satisfied. Discretizations of conservation equations via finite differences rely on the differential form, and artificial viscosity must be added near shock fronts, forcing q to be differentiable. An alternate strategy is to develop numerical algorithms based directly on the integral formulation of the conservation laws. The Godunov method and its extensions are examples of this latter approach, and are the topic of the next section.

3.2. Godunov's method

Numerical algorithms for conservation laws are developed by discretizing the equations in their fundamental integral form. These methods derive from a *control volume* discretization, whereby the domain is divided into *computational* cells, C_i , now defined to span the interval $[x - \Delta x/2, x + \Delta x/2] \equiv [x_{i-1/2}, x_{i+1/2}]$, where Δx is the (local) spatial discretization scale. Following the derivation of the integral conservation law (53) for the computation cell C_i , we introduce the *averaged* quantities, \bar{q}_i^n :

$$\bar{q}_i^n = \frac{1}{\Delta x} \int_{x_{i-1/2}}^{x_{i+1/2}} dx q(x, t_n), \quad (55)$$

with $t_n \equiv n \Delta t$, where Δt is the temporal discretization scale. We then obtain the discrete form of the conservation law (53)

$$\bar{q}_i^{n+1} = \bar{q}_i^n - \frac{\Delta t}{\Delta x} (F_{i+1/2} - F_{i-1/2}), \quad (56)$$

where the 'numerical flux' is defined by

$$F_{i+1/2} = \frac{1}{\Delta t} \int_{t_n}^{t_{n+1}} dt f(q(x_{i+1/2}, t)). \quad (57)$$

At first sight, a numerical method based on a discretization of the integral conservation law does not appear promising: the flux integral (57) does not appear readily solvable, and it generally is not. However, in his seminal work, Godunov [17] devised a technique to approximately evaluate the flux integral by replacing the function $q(x, t_n)$ with $\tilde{q}(x, t_n)$, where $\tilde{q}(x, t_n)$ is a piecewise constant function. In this approach, the individual cells ('control volumes') are treated as a sequence of 'shock tubes', and a separate Riemann initial value problem is solved at each cell interface. Provided that the waves from neighbouring cells do not interact—a proviso which gives a Courant-type condition on the time step—each Riemann problem can be solved exactly to yield the local solution $\tilde{q}(x, t)$ (for $t > t_n$) for each 'shock tube'. Furthermore, since the solution of each of the local Riemann problems is self-similar, $\tilde{q}(x_{i+1/2}, t)$ is a constant in time, and the evaluation of the integral (57) becomes trivial. This then allows one to find explicit expressions for the cell averages at the advanced time, \bar{q}^{n+1} , via (56). In summary, the Godunov method proceeds as follows: (a) from the average \bar{q}_i^n , one 'reconstructs' a piecewise constant function $\tilde{q}(x, t_n)$ to approximate the solution in C_i ; (b) the Riemann problem is solved at the interfaces between cells, giving the solution $\tilde{q}(x, t)$ for $t_n < t \leq t_{n+1}$; (c) the solution $\tilde{q}(x, t_{n+1})$ is averaged over the cell C_i to obtain the average at the advanced time, \bar{q}_i^{n+1} . We note that methods for solving the Riemann problem exactly for relativistic fluids have been given by Smoller and Temple [21] for the ultrarelativistic EOS and by Martí and Müller [22] for the ideal-gas EOS.

Godunov's method has many nice properties: in particular, it is conservative and allows for the stable evolution of strong shocks. However, the original scheme *does* have some shortcomings: convergence is only first order, and the exact solution of the Riemann problem may be computationally expensive, especially for relativistic fluids. The convergence of the scheme can be improved by providing a more sophisticated reconstruction $\tilde{q}(x, t_n)$, giving what are known as *high-resolution shock-capturing* methods. One such procedure is described in section 3.3, with details concerning the scheme's convergence given in section 4.7. In order to address the issue of computational efficiency, approximate Riemann solvers have been developed that relate the problem-at-hand to a simpler system for which the Riemann problem is easier to solve. Several approximate Riemann solvers have been developed for classical fluid dynamics, and many of these approximate methods have been extended to relativistic fluid systems. These include relativistic two-shock solvers [23, 24], a relativistic Harten–Lax–van-Leer–Einfeldt (HLL) solver [25] and, as discussed in section 3.4, various linearized solvers.

3.3. Cell reconstruction

Godunov-type numerical methods are based on solutions of the Riemann initial value problem at the interfaces between cells. As discussed above, during an update step one introduces functions $\tilde{q}(x, t)$ (defined piecewise on the intervals $[x_{i-1/2}, x_{i+1/2}]$) to approximate the solution in the control volumes C_i . These functions are created from the cell averages \bar{q}_i^n , and hence are called *reconstructions*. Consider the cell interface at $x_{i+1/2}$: the state of the fluid immediately to the right (left) is $\tilde{q}_{i+1/2}^r$ ($\tilde{q}_{i+1/2}^l$). The simplest reconstruction is to assume that \tilde{q} is piecewise constant

$$\tilde{q}_{i+1/2}^l = \bar{q}_i, \quad \tilde{q}_{i+1/2}^r = \bar{q}_{i+1}, \quad (58)$$

as used in the original Godunov method and, as already discussed, this reconstruction results in a numerical scheme in which the spatial derivatives (and hence the overall scheme) have first-order accuracy. The convergence can be improved by using a higher-order reconstruction

for \tilde{q} , but care must be exercised so that the reconstruction does not induce spurious oscillations near discontinuities (see figure 2).

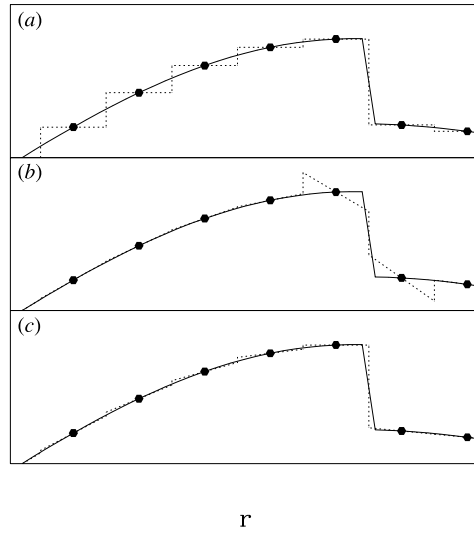


Figure 2. The three frames of this plot show the different ways in which a discretized function can be reconstructed in a control-volume numerical method. The full curve represents a continuum (or ‘analytic’) function and the full hexagons represent discrete, approximate values of the function defined at grid points. Frame (a) represents the piecewise constant reconstruction. Frame (b) shows a naive piecewise linear reconstruction of each cell using $s_{i+1/2}$. This reconstruction oscillates near discontinuities in the function—such oscillations can easily lead to instabilities. Frame (c) shows a piecewise linear reconstruction performed with the minmod limiter as described in the text. This reconstruction produces a discrete representation of the dynamical variable which remains well behaved near discontinuities.

We have chosen to use a piecewise *linear* reconstruction for \tilde{q} , which formally results in a scheme with second-order convergence. (The convergence properties are discussed further in section 4.7.) The \tilde{q} are reconstructed using the total variation diminishing (TVD) minmod limiter introduced by van Leer [26]. The minmod limiter forces \tilde{q} to be monotonic near discontinuities, and this reduces the (local) accuracy of the scheme to first order. The first step of the reconstruction algorithm involves the computation of the slope (derivative of the dynamical variable) centred at the cell boundaries

$$s_{i+1/2} = \frac{\tilde{q}_{i+1} - \tilde{q}_i}{r_{i+1} - r_i}. \quad (59)$$

A ‘limited slope’, σ_i , is then calculated via

$$\sigma_i = \text{minmod}(s_{i-1/2}, s_{i+1/2}), \quad (60)$$

where the minmod function is defined by

$$\text{minmod}(a, b) = \begin{cases} a & \text{if } |a| < |b| \text{ and } ab > 0 \\ b & \text{if } |b| < |a| \text{ and } ab > 0 \\ 0 & \text{if } ab < 0. \end{cases} \quad (61)$$

Using the limited slopes, we evaluate \tilde{q} at the cell interfaces as follows:

$$\tilde{q}_{i+1/2}^\ell = \tilde{q}_i + \sigma_i (r_{i+1/2} - r_i) \quad (62)$$

and

$$\tilde{q}_{i+1/2}^r = \bar{q}_{i+1} + \sigma_{i+1}(r_{i+1/2} - r_{i+1}). \quad (63)$$

After calculating the conservative variables at the interface, we then calculate the corresponding primitive variables, \tilde{w}^ℓ and \tilde{w}^r . Owing to the finite-precision nature of our computations, we sometimes are unable to calculate physical values for these primitive variables, and here we revert to a piecewise constant reconstruction for \tilde{q}^ℓ and \tilde{q}^r .

3.4. The Roe linearized solver

Perhaps the most popular approximate Riemann solver is the linearized solver introduced by Roe [27]. This solver (and subsequent variants) has been used in a variety of applications involving general relativistic fluids [28–33], and has proven to be robust and efficient. (The efficiency comparison is relative to solving either the exact Riemann problem for relativistic fluids, or a nonlinear approximation, such as the two-shock solver.) As the name suggests, the linearized solver approximates the full nonlinear problem by replacing the nonlinear equations by *linear* systems defined at each cell interface. The associated linear Riemann problems can then be solved exactly and cheaply, and the resulting solutions can be pieced together to produce an approximation to the solution of the original, nonlinear equations.

The key idea is to first write the nonlinear system in *quasilinear* form

$$\partial_t \mathbf{q} + \mathcal{A}(\mathbf{q}) \partial_x \mathbf{q} = 0. \quad (64)$$

Here, \mathcal{A} is an $M \times M$ matrix which is now a function of \mathbf{q} . Roe [27] gives three specific criteria for the construction of \mathcal{A} :

- (a) $\mathcal{A}(\tilde{q}^\ell, \tilde{q}^r)(\tilde{q}^r - \tilde{q}^\ell) = \mathbf{f}(\tilde{q}^r) - \mathbf{f}(\tilde{q}^\ell)$;
- (b) $\mathcal{A}(\tilde{q}^\ell, \tilde{q}^r)$ is diagonalizable with real eigenvalues;
- (c) $\mathcal{A}(\tilde{q}^\ell, \tilde{q}^r) \rightarrow \mathbf{f}'(\mathbf{q})$ smoothly as $\tilde{q}^\ell, \tilde{q}^r \rightarrow \mathbf{q}$.

The latter two criteria can generally be satisfied by letting \mathcal{A} be the Jacobian matrix evaluated using the arithmetic average of the conservative variables at the interface:

$$\mathcal{A} = \left. \frac{\partial \mathbf{f}(\mathbf{q})}{\partial \mathbf{q}} \right|_{\mathbf{q}=\bar{\mathbf{q}}_{i+1/2}}, \quad (65)$$

where

$$\bar{\mathbf{q}}_{i+1/2} = \frac{1}{2}(\tilde{\mathbf{q}}_{i+1/2}^\ell + \tilde{\mathbf{q}}_{i+1/2}^r). \quad (66)$$

While this construction does not generally satisfy the first criterion, equation (65) is often used in relativistic fluid dynamics (see, for example, [28,30,33]) on the basis of its relative simplicity, and we also adopt this approach. On the other hand, other authors [29] have constructed a linearized Riemann solver for relativistic fluids with true Roe averaging, and we therefore refer to our scheme as a ‘quasi-Roe’ method.

Having defined a specific linearization, the scheme proceeds by evaluation of $\mathcal{A}(\bar{\mathbf{q}}_{i+1/2})$, which is now viewed as a matrix with (piecewise) constant coefficients, followed by the solution of the Riemann problem for the resulting linear system. Carrying through an analysis not given here (see, e.g., [18]), the Roe flux can be defined as

$$\mathbf{F}_{i+1/2} = \frac{1}{2} \left[\mathbf{f}(\tilde{\mathbf{q}}_{i+1/2}^r) + \mathbf{f}(\tilde{\mathbf{q}}_{i+1/2}^\ell) - \sum_{\mu} |\lambda_{\mu}| \Delta \omega_{\mu} \mathbf{r}_{\mu} \right], \quad (67)$$

where, again, λ_μ and \mathbf{r}_μ are the eigenvalues and (right) eigenvectors, respectively, of $\mathcal{A}(\bar{\mathbf{q}}_{i+1/2})$. The quantities $\Delta\omega_\mu$ are defined in terms of the jumps in the fluid variables across the interface

$$\tilde{\mathbf{q}}_{i+1/2}^r - \tilde{\mathbf{q}}_{i+1/2}^\ell = \sum_\mu \Delta\omega_\mu \mathbf{r}_\mu. \tag{68}$$

For completeness, we give explicit expressions for the eigenvectors and eigenvalues of the ultrarelativistic fluid system (31) in appendix A.

Finally, it is important to remember that approximate Riemann solvers produce approximate solutions, which, under certain conditions, may diverge from the physical solutions. For example, concentrating on the Roe solver, Quirk [34] has recently reviewed several ‘subtle flaws’ in approximate solvers. Fortunately, the approximate solvers often fail in different ways, and where one solver produces an unphysical solution, another solver may give the physical solution. Thus, it may be necessary to investigate a particular problem with multiple approximate Riemann solvers. Therefore, we have also implemented Marquina’s solver [35], an alternative linear solver that has also found application in relativistic fluid studies [33, 36], as an option in our code. In addition to using the quasi-Roe and Marquina solvers to investigate the critical collapse of perfect fluids, we also implemented the HLLC solver in an independent code. We found that the quasi-Roe solver gave accurate solutions, and provided the best combination of resolution and efficiency for the critical collapse problem. Consequently, the results presented in [12] were obtained with this solver.

4. Solving the Einstein/fluid system

This section deals with some details of our numerical solution of the coupled Einstein/fluid equations, including the incorporation of source terms into our conservation laws, regularity and boundary conditions, and methods for calculating physical values for w in the ultrarelativistic regime. In addition, we describe the initial data and mesh structure we have used in our studies of critical phenomena in fluid collapse. Finally, we conclude the section with some remarks on how we have tested and validated our code. The full details of our numerical scheme are presented in appendix B.

4.1. Time integration

In section 2.4 the fluid equations of motion were written essentially in conservative form, except that a source term, ψ , had to be included. While this source term clearly breaks the strict conservative form of the equations, it can be incorporated self-consistently into our numerical scheme by using the method of lines to discretize space and time separately. (For additional information on the method of lines see Thornburg [37] and references therein.) Specifically, the discretized fluid equations become

$$\frac{d\bar{\mathbf{q}}_i}{dt} = -\frac{1}{r_i^2 \Delta r} [(r^2 X \mathbf{F})_{i+1/2} - (r^2 X \mathbf{F})_{i-1/2}] + \psi(\bar{\mathbf{q}}_i), \tag{69}$$

where $\bar{\mathbf{q}}_i$ is the cellular average of \mathbf{q} , $\mathbf{F}_{i\pm 1/2}$ are the numerical fluxes defined by (67), and $X = \alpha/a$, as previously. These equations can be integrated in time using standard techniques for ordinary differential equations (ODEs). In particular, Shu and Osher [38] have investigated different ODE integration methods, and have found that the modified Euler method (or Huen’s method) is the optimal second-order scheme consistent with the Courant condition required

for a stable evolution. We briefly digress to define this scheme for a general set of differential equations of the form

$$\frac{dq}{dt} = L(q), \quad (70)$$

where L is a spatial differential operator. Let q^n be the *discretized* solution at time $t = n\Delta t$, and \hat{L} be the discretized differential operator. The modified Euler method is a predictor–corrector method, with predictor

$$q^* = q^n + \Delta t \hat{L}(q^n), \quad (71)$$

and corrector

$$q^{n+1} = \frac{1}{2}(q^n + q^*) + \frac{1}{2}\Delta t \hat{L}(q^*). \quad (72)$$

Again, we note that Δt is subject to a Courant (CFL) condition, which can be deduced empirically or possibly from a linearized stability analysis.

Particularly in comparison with the treatment of the fluid equations, the numerical solution of the equations governing the geometric quantities α and a is straightforward. As discussed previously, the lapse, α , is fixed by the polar slicing condition (18), while a can be found from either the Hamiltonian (19) or momentum (17) constraints. We have used discrete, second-order, versions of both equations for a , and have obtained satisfactory results in both cases (the polar slicing equation is likewise solved using a second-order scheme). In general, however, (and particularly on vector machines) solution via the momentum constraint yields a far more efficient scheme, and we thus generally use the momentum equation to update a .

4.2. Regularity and boundary conditions

In the polar-areal coordinate system, the lapse ‘collapses’ exponentially near an apparent horizon, preventing the $t = \text{constant}$ surfaces from intersecting the physical singularity which must develop interior to a black hole. As the slices ‘avoid’ the singularity, elementary flatness holds at the origin for all times in the evolution, giving

$$a(0, t) = 1. \quad (73)$$

At each instant of time, the polar-slicing condition (18) determines the lapse only up to an overall multiplicative constant, reflecting the reparametrization invariance, $t \rightarrow \tilde{t}(t)$, of the polar slices. We chose to normalize the lapse function so that as $r \rightarrow \infty$, coordinate time corresponds to proper time. On a finite computational domain, and provided no matter out-fluxes from the domain, this condition is approximated via

$$\alpha a|_{r_{\max}} = 1. \quad (74)$$

The regularity conditions for the fluid are imposed on the variables S and τ . In spherical symmetry the fluid flows along radial lines, and given that there are no sources or sinks at the origin, we have that $v(0, t) = S(0, t) = 0$. Regularity at the origin further requires τ to have an even expansion in r as $r \rightarrow 0$:

$$\tau(r, t) = \tau_0(t) + r^2\tau_2(t) + O(r^4). \quad (75)$$

On our radial grid r_i , $i = 1, 2, \dots, N$, we use this expansion to compute grid-function values defined at $r = r_1 = 0$ in terms of values defined at $r = r_2$ and $r = r_3$. Specifically, once the

values Φ_2 and Φ_3 have been updated via the equations of motion, we compute τ_2 and τ_3 , and then calculate τ_1 using the ‘quadratic fit’ based on the expansion (75)

$$\tau_1 = \frac{\tau_2 r_3^2 - \tau_3 r_2^2}{r_3^2 - r_2^2}. \tag{76}$$

Once τ is determined at the origin, we set Π_1 and Φ_1 .

At the outer boundary we apply out-flow boundary conditions, which in our case are simply first-order extrapolations for Π and Φ :

$$\Phi_N = \Phi_{N-1} \quad \Pi_N = \Pi_{N-1}. \tag{77}$$

In addition, two ghost cells ($r = r_{N+1}, r = r_{N+2}$) are added at the outer edge of the grid for ease in coding the cellular reconstruction algorithm [19]. These ghost cells are also updated with first-order extrapolation.

4.3. Floor

The fluid model is a continuum approximation, and, at least naively, the fluid equations become singular as $\rho \rightarrow 0$. In these evacuation regions, both the momentum and mass density are very small, and therefore the velocity—which loosely speaking is the quotient of the two—is prone to fractionally large numerical errors. These errors often result in the computation of unphysical values for the fluid variables, such as supraluminal velocities, negative pressures or negative energies. (In addition, of course, our code must contend with the usual discretization and round-off errors common to any numerical solution of a set of PDEs.) At least from the point of view of Eulerian fluid dynamics, it seems fair to say that a completely satisfactory resolution of the evacuation problem does not exist. In the absence of a mathematically rigorous and physically acceptable procedure, we adopt the *ad hoc* approach of demanding that $\rho > 0$ everywhere on the computational domain, i.e. we exclude the possibility that vacuum regions can form on the grid. In terms of our conservative variables \mathbf{q} , this requirement becomes $\Pi > 0$ and $\Phi > 0$. In a wide variety of situations, our numerical solutions of the fluid equations naturally satisfy these constraints. However, the critical solutions for ‘stiff’ equations of state ($\Gamma \gtrsim 1.9$) develop extremely relativistic velocities ($W > 10^6$) in regions where ρ is small [12], and we are unable to solve the fluid PDEs in these cases without imposing *floor* (or minimum) values on \mathbf{q} . Specifically, at each step in the integration we require

$$\Pi \geq \delta, \quad \Phi \geq \delta, \tag{78}$$

where the floor δ is chosen to be several orders of magnitude smaller than the density associated with what we feel are the physically relevant features of the solution—a typical value is $\delta = 10^{-10}$. The floor is often applied in regions where Π and Φ differ greatly in magnitude, and discretization errors can easily lead to the calculation of a negative value for either function. For example, the floor may be applied to the ‘in-going’ function in a region where the fluid is overwhelmingly ‘out-going’. In these cases, the effect of the floor is dynamically unimportant. However, the floor may be invoked in other cases, where its effect on the dynamics is less certain.

Given the *ad hoc* nature of this regularization procedure, the crucial question is whether the floor affects the computed solutions in a substantial way. We investigated this question by comparing near-critical solutions for $\Gamma = 2$ (the most extreme case) which were calculated at the same resolution with three distinct floor values: $\delta = 10^{-6}$, $\delta = 10^{-8}$, and our usual $\delta = 10^{-10}$. These tests indicated that the calculation of $\Gamma = 2$ critical solutions and measurements of the mass-scaling parameter are not sensitive to the *magnitude* of the floor,

and additional information is given in appendix C. However, the mere presence of a non-zero floor may affect the $\Gamma = 2$ solution. This can be seen by comparing the full PDE solution with the continuously self-similar ODE solution, as discussed further in the companion paper [12]. Finally, the use of a floor makes estimates of the maximum Lorentz factor attained in the critical solutions unreliable because the largest velocities occur in regions where the floor is enforced.

4.4. Calculating the velocity

The simple expression (27) for v in terms of q , when used naively with finite-precision arithmetic, can result in the computation of unphysical, supraluminal velocities. For example, when searching for critical solutions we routinely calculate fluid flows with $W \gtrsim 10^3$. Thus, when calculating v from the quotient (27), small numerical errors can easily conspire to give $|v| \geq 1$, rather than the correct $|v| \gtrsim 0.999999$. On the other hand, the combination

$$\chi \equiv W^2 v \quad (79)$$

is insensitive to small numerical errors, and provides a better avenue for calculating v from the conservative variables. From the definition (15) of S and the equation of state we have

$$\chi = \frac{(\Gamma - 1) S}{\Gamma P}. \quad (80)$$

The velocity can then be calculated from χ using

$$v = \frac{1}{2\chi} (\sqrt{1 + 4\chi^2} - 1). \quad (81)$$

To the limit of machine precision, v is then in the physical range $-1 < v < 1$. When $\chi \ll 1$, we calculate v from a Taylor expansion of (81), although (27) could also be used. We also use χ when calculating w from q for the ideal-gas EOS (10).

4.5. Grid

The black-hole-threshold critical solutions—which are our primary focus—are generically self-similar, and as such, require an essentially unbounded dynamical range for accurate simulation. Thus some sort of adaptivity in the construction of the computational domain is crucial, and, indeed, the earliest studies of critical collapse [1] used Berger–Oliger adaptive mesh refinement [39] to great advantage. However, in contrast to the early work, we know (at least schematically) the character of the critical solutions we seek, and thus we can, and have, use this information to construct a simple, yet effective, adaptive grid method. (Our approach is similar in spirit to that adopted by Garfinkle [40] in his study of scalar field collapse.) Specifically, at any time during the integration our spatial grid has three distinct domains: the two regions near $r = 0$ and r_{\max} have uniform grid spacings (but the spacing near $r = 0$ is typically *much* smaller than that near the outer edge of the computational domain), and the intermediate region has grid points distributed uniformly in $\log(r)$ (see figure 3). As a near-critical solution propagates to smaller spatial scales, additional grid points are added in order to maintain some given number of grid points between $r = 0$ and some identifiable feature of the critical solution. For example, we typically require that at least 300 or so grid points lie between the origin and the maximum of the profile of the metric function a .

The primary advantage of this gridding scheme is that it is simple to implement, and yet allows us to resolve detail over many length scales: the ratio of the grid spacing at the outer edge to the spacing at the origin is typically 10^{10} – 10^{13} at the end of an evolution. The primary

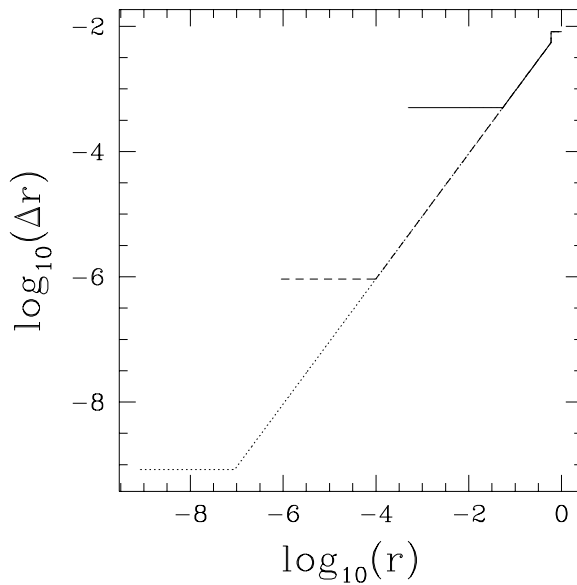


Figure 3. Illustration of the remeshing algorithm used in investigations of critical collapse. The grid spacing Δr is shown as a function of r on a log–log plot. The full line represents the initial grid, the dotted line shows the grid spacing after the first addition of points near the origin and the broken line shows the grid spacing after the second regridding. Note that the grid spacings near the origin, and near the outer edge of the computational domain are uniform (horizontal lines). At each regridding cycle, the grid spacing near the origin is halved, and the new points are matched smoothly onto the previous grid. A critical evolution may involve more than 20 regriddings, although only a small number of points (50–150) may be added at a time.

disadvantage of this scheme is that it is specialized for critical collapse, and cannot be used for more general physical problems.

4.6. Initial data for critical solutions

We expect that the critical solutions in fluid collapse will be universal, in the sense that *any* family of initial data which generates families that ‘interpolate’ between complete dispersal and black-hole formation, should exhibit the same solution at the black-hole threshold. We have thus focused attention on a specific form of initial data, which generates initially imploding (or imploding/exploding) shells of fluid. Specifically, the energy density in the shells has a Gaussian profile,

$$\tau = \tau_0 \exp[-(r - r_0)^2/\Delta^2] + K, \quad (82)$$

where the constant K —typically of magnitude $10^{-6}\tau_0$ —represents a constant ‘background’ fluid. It should be noted that this background is used only in setting the initial data, and is not held fixed during the evolution—in particular, K is *not* a floor as discussed in section 4.3. The shells are either time-symmetric, or have an initial inward velocity which is proportional to r . Critical solutions were found by fixing r_0 and Δ , and then tuning the pulse amplitude τ_0 .

4.7. Tests

When developing a code such as the one described here, a variety of tests can be used to verify that the code is producing reliable results. For example, independent residual tests

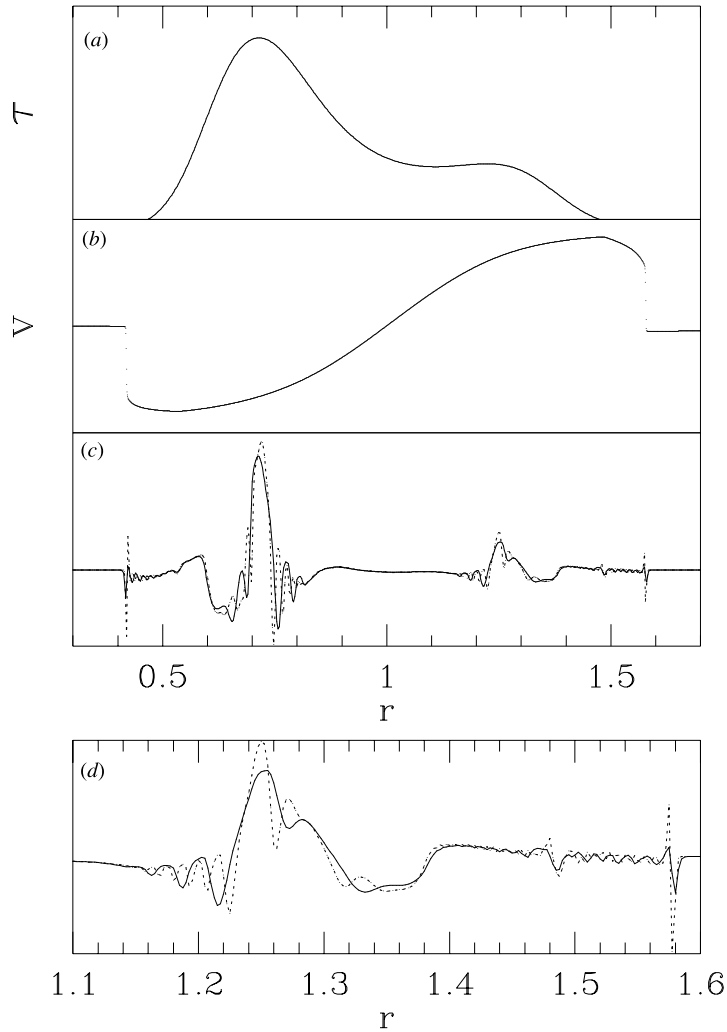


Figure 4. Illustration of some of the convergence properties of the solution algorithm discussed in the text. Here we evolved a time-symmetric shell of fluid ($\Gamma = 1.3$) using uniform grids with three different resolutions: $\Delta r = h, 2h$ and $4h$ in the weak gravitational field limit. Convergence is investigated by comparing the solutions obtained using the three distinct discretization scales. In frame (c), the full curve is $(\tau_{2h} - \tau_{4h})$ and the dotted curve is $4(\tau_h - \tau_{2h})$, where the subscript on τ indicates the grid spacing for a particular solution. When the convergence is second order, the two curves should (roughly) coincide, while when the convergence is first order, the amplitude of the dotted curve should be twice that of the full curve. As expected, we see that the convergence is not second order at the shock. (Of course the whole notion of convergence at a discontinuity fails, as the notion of Richardson expansion requires smooth functions.) However, we also can see that the convergence is only first order at the extrema of q —at these points, the slope changes sign, and the minmod limiter produces a first-order reconstruction. Frame (d) shows a more detailed view of a portion of the data displayed in (c). For context, we also show τ in frame (a) and v in frame (b).

and comparisons with exact solutions can be used to ensure that the code is solving the correct differential equations, and that it is producing ‘physical’ solutions. Arguably the most fundamental, useful and universally applicable testing technique is convergence testing, which generally demonstrates that the numerical method is consistent and has been correctly

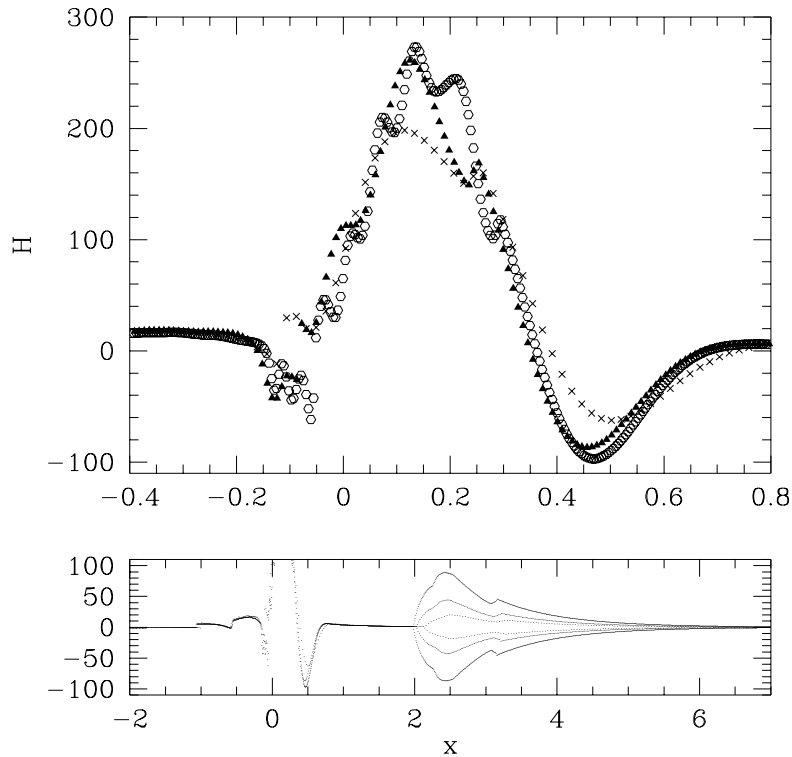


Figure 5. Convergence behaviour of, H^h , the residual of the Hamiltonian constraint, for a $\Gamma = 1.9$ sub-critical evolution near the threshold of black-hole formation. Computations were run at resolutions, $4h$ (crosses), $2h$ (triangles) and h (circles); we plot $16H^h$, $4H^{2h}$ and H^{4h} , so that second-order convergence is signalled by near coincidence of the plotted data sets. The specific residuals shown are calculated on the adaptive log grid at a time just before the fluid disperses from the origin. (The x coordinate is a logarithmic coordinate proportional to $\ln r$, and is defined in [12].) The top frame shows the scaled residuals in the neighbourhood of the ‘critical part’ of the solution (i.e. the strong-field, nonlinear, dynamical region), while the lower frame shows the scaled residuals for an expanded region of the domain. The $O(h^2)$ convergence of our code in the strong-field, critical regime is apparent, as is a region of first-order convergence in the region exterior to the critical evolution. This latter region appears to be a transition between a segment of the grid where the floor is inactive ($x < 2$, at the time plotted), and a segment where the floor is continuously applied ($x > 3.5$). In the intermediary region, the floor is active every second grid point. In any case, it must be stressed that the dynamical variables in the transition region have sizes of order of their respective floors, i.e. in the $O(h)$ region, the dynamical variables are orders of magnitude smaller than they are in the strong-field, $O(h^2)$ regime, and are also orders of magnitude smaller than the typical level of global error in the solutions.

implemented, but which also provides an *intrinsic* method for estimating the level of error in a given numerical solution. This section discusses the convergence properties of our code, focusing especially on convergence in the critical regime of a collapsing fluid. Some additional tests are discussed in appendix C.

For our high-resolution shock-capturing scheme, a general rule-of-thumb is that the convergence should be (apparently) second order where the flow is smooth, and first order at discontinuities, where the effects of the slope limiter become important. In addition, we can also expect first-order convergence near extrema of \bar{q} , since at these points, the slope, s , changes sign, and the minmod limiter gives a piecewise constant

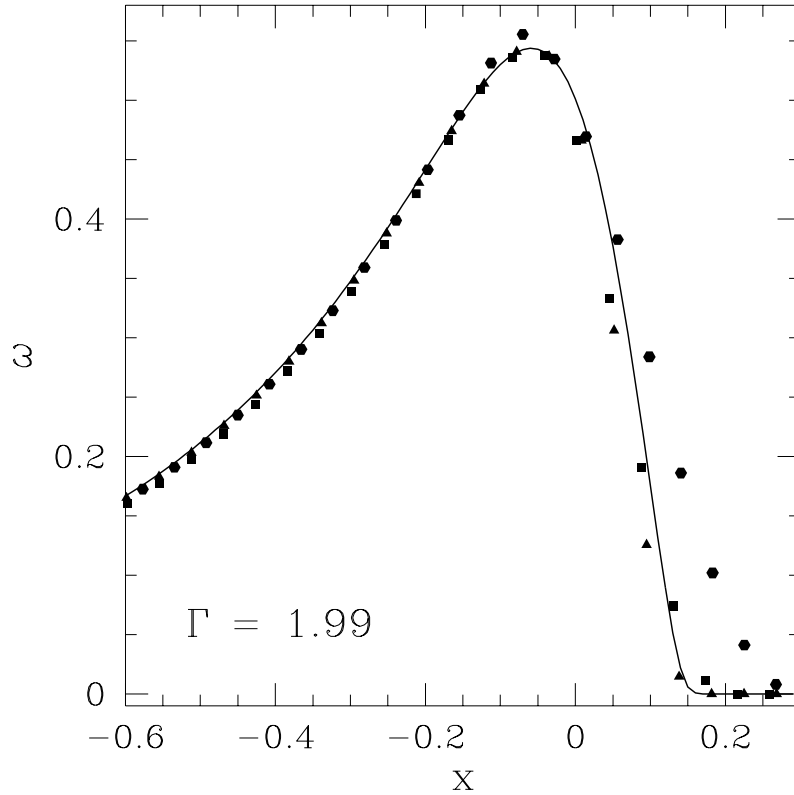


Figure 6. The convergence behaviour of ω for the $\Gamma = 1.99$ critical solution, where $\omega \equiv 4\pi a^2 r^2 \rho$ and the independent variable x is proportional to $\ln r$. The full curve shows the exact solution, obtained by numerically integrating ODEs obtained from the continuously self-similar ansatz [12]. The points show ω^h calculated using our Einstein/fluid code at three spatial resolutions, h (triangles), $2h$ (squares), and $4h$ (hexagons). (These resolution ratios are approximate, given the logarithmic basis of the grid.)

reconstruction for \tilde{q} . A convergence test where these effects are apparent is shown in figure 4.

Our fluid code has been primarily optimized for studying perfect-fluid critical solutions. These solutions are continuously self-similar, smooth, very dynamic and exist in the strong-field limit of general relativity. Thus the most important—and demanding—test is a convergence test of a near-critical solution at the verge of black-hole formation. We found the critical solutions for a $\Gamma = 1.9$ fluid at three different resolutions, and plotted the residual of the Hamiltonian constraint in figure 5. (Recall that the momentum constraint is used to update a , so the Hamiltonian constraint gives an independent check of the solutions.) While the convergence of our scheme reverts to first order at the extrema of $\{\Pi, \Phi\}$, which occur at $r = 0$ for a collapsing perfect fluid, the region most interesting for studying critical solutions is near the maximum of $r^2\tau$, where the convergence is second order. Finally, we obtain the $\Gamma = 1.99$ critical solution using our Einstein/fluid code at three different spatial resolutions, and compare these solutions to the exact solution. Figure 6 compares these solutions using the variable ω ($\omega \equiv 4\pi a^2 r^2 \rho$), showing that the PDE solutions converge to the exact solution.

5. Conclusion

In this paper we give a detailed description of an Eulerian evolution code for spherically symmetric, general-relativistic, perfect-fluid collapse, optimized for the study of black-hole-threshold (critical) behaviour. The paper includes: (a) the equations of motion solved by the code; (b) the quasi-Roe numerical method for solving the fluid equations; (c) techniques used to maintain physical primitive fluid variables throughout the evolution; (d) a description of the adaptive spatial grid; (e) regularity and boundary conditions for the fluid variables; and (f) the discretization of all equations. The critical solutions contain a central region of collapsing fluid and an exploding fluid in the outer region, where the fluid velocities approach the speed of light, making these solutions both dynamic and extremely relativistic. We find that the introduction of the new fluid variables, $\{\Pi, \Phi\}$, and the very careful transformation from conservative to primitive variables are crucial for a successful—and thorough—study of stiff ($\Gamma \gtrsim 1.9$) perfect-fluid critical behaviour. We also present several tests of our code, most importantly demonstrating convergence for the dynamic fluid at the threshold of black-hole formation. The results of our critical behaviour studies are presented in the companion paper [12].

Acknowledgments

This work was supported in part by the National Science Foundation under grants PHY93-18152 (ARPA supplemented), PHY94-07194, PHY97-22068, by a Texas Advanced Research Project grant, and by an NPACI award of computer time. It was also supported by the Canadian Institute for Advanced Research and by NSERC. We thank Carsten Gundlach for interesting discussions, and for suggestions on improving a preliminary version of this paper. MWC gratefully acknowledges the hospitality of the Institute for Theoretical Physics, UC Santa Barbara, where part of this research was carried out.

Appendix A. Characteristic structure

In this appendix we calculate the Jacobian matrix \mathcal{A} for the relativistic fluid equations, and then compute the associated eigenvalues and right eigenvectors. The flat-space components of \mathcal{A} are

$$\mathcal{A}_{11} = \frac{1}{2}(1 + 2v - v^2) + (1 - v^2) \frac{\partial P}{\partial \Pi} \quad (\text{A1})$$

$$\mathcal{A}_{12} = -\frac{1}{2}(v + 1)^2 + (1 - v^2) \frac{\partial P}{\partial \Phi} \quad (\text{A2})$$

$$\mathcal{A}_{21} = \frac{1}{2}(v - 1)^2 + (v^2 - 1) \frac{\partial P}{\partial \Pi} \quad (\text{A3})$$

$$\mathcal{A}_{22} = \frac{1}{2}(-1 + 2v + v^2) + (v^2 - 1) \frac{\partial P}{\partial \Phi}, \quad (\text{A4})$$

and the partial derivatives of P are easily found from (33). The eigenvalues λ_{\pm} of \mathcal{A} are the two roots of the quadratic equation

$$\lambda^2 - (\mathcal{A}_{11} + \mathcal{A}_{22})\lambda + \det \mathcal{A} = 0, \quad (\text{A5})$$

and the right eigenvectors are

$$\mathbf{r}_\pm = \begin{pmatrix} 1 \\ Y_\pm \end{pmatrix}, \quad (\text{A6})$$

where

$$Y_\pm \equiv \frac{\lambda_\pm - \mathcal{A}_{11}}{\mathcal{A}_{12}}. \quad (\text{A7})$$

If the eigenvalues are numerically degenerate owing to the limitations of finite-precision arithmetic, we set $\lambda_\pm = 0$. When $\Gamma = 2$, the eigenvalues and eigenvectors become simply

$$\lambda_\pm = \pm 1, \quad \mathbf{r}_+ = \begin{pmatrix} 1 \\ 0 \end{pmatrix}, \quad \mathbf{r}_- = \begin{pmatrix} 0 \\ 1 \end{pmatrix}, \quad (\Gamma = 2). \quad (\text{A8})$$

Appendix B. Implementation details

The origin in spherical symmetry requires additional care because powers of $1/r$ appear in the flux and source terms. One particular difficulty results from the partial cancellation of the source term, $2\alpha P/(ar)$, with the pressure term in the flux. Numerically this cancellation is not exact, and this non-cancellation can induce large errors near the origin. We therefore modify the difference equations in order to eliminate the offending term. We first decompose the numerical flux into two parts $\mathbf{f}^{(1)}$ and $\mathbf{f}^{(2)}$:

$$\mathbf{f}^{(1)} = \begin{bmatrix} \frac{1}{2}(\Pi - \Phi)(1 + v) \\ \frac{1}{2}(\Pi - \Phi)(1 - v) \end{bmatrix}, \quad \mathbf{f}^{(2)} = \begin{bmatrix} P \\ -P \end{bmatrix}, \quad (\text{B1})$$

so that $\mathbf{f} = \mathbf{f}^{(1)} + \mathbf{f}^{(2)}$. We then rewrite the conservation equations (24) with these new fluxes as

$$\partial_t \mathbf{q} + \frac{1}{r^2} \partial_r (r^2 X \mathbf{f}^{(1)}) + \partial_r (X \mathbf{f}^{(2)}) = \hat{\Sigma}, \quad (\text{B2})$$

where the new source term $\hat{\Sigma}$ is

$$\hat{\Sigma} = \begin{bmatrix} \Theta \\ -\Theta \end{bmatrix}. \quad (\text{B3})$$

The numerical flux function \mathbf{F} is similarly decomposed: $\mathbf{F} = \mathbf{F}^{(1)} + \mathbf{F}^{(2)}$, with

$$\mathbf{F}_{i+1/2}^{(1)} = \frac{1}{2} \left[\mathbf{f}^{(1)}(\tilde{q}_{i+1/2}^\ell) + \mathbf{f}^{(1)}(\tilde{q}_{i+1/2}^r) - \sum_\mu |\lambda_\mu| \Delta \omega_\mu \mathbf{r}_\mu \right], \quad (\text{B4})$$

$$\mathbf{F}_{i+1/2}^{(2)} = \frac{1}{2} [\mathbf{f}^{(2)}(\tilde{q}_{i+1/2}^\ell) + \mathbf{f}^{(2)}(\tilde{q}_{i+1/2}^r)]. \quad (\text{B5})$$

The finite-differencing of the flux terms is adapted so that the derivatives have the correct leading-order behaviour near the origin. From the regularity conditions discussed in section 4.2 we have

$$\lim_{r \rightarrow 0} r^2 X \mathbf{f}^{(1)} \propto r^3, \quad \lim_{r \rightarrow 0} X \mathbf{f}^{(2)} \propto \text{constant}, \quad (\text{B6})$$

and we thus write the discretized equations of motion as

$$\frac{d\bar{q}_i}{dt} = - \frac{3[(r^2 X \mathbf{F}^{(1)})_{i+1/2} - (r^2 X \mathbf{F}^{(1)})_{i-1/2}]}{r_{i+1/2}^3 - r_{i-1/2}^3} - \frac{(X \mathbf{F}^{(2)})_{i+1/2} - (X \mathbf{F}^{(2)})_{i-1/2}}{r_{i+1/2} - r_{i-1/2}} + \hat{\Sigma}_i. \quad (\text{B7})$$

The geometric equations are differenced using standard second-order finite-difference techniques. The momentum constraint is

$$\frac{da_i}{dt} = 2\pi r_i \alpha_i a_i^2 (\Pi_i - \Phi_i), \quad (\text{B8})$$

and is integrated using the modified Euler method described in section 4.1. The discretized polar slicing condition (18) in discrete form is

$$(\ln \alpha)_{i+1}^n = (\ln \alpha)_i^n + \Delta r \left\{ a \left[2\pi r ((\Pi - \Phi)v + P) + \frac{1}{2r} \left(1 - \frac{1}{a^2} \right) \right] \right\}_{i+1/2}^n, \quad (\text{B9})$$

where all of the basic variables (a , Π , Φ , v and P) in the $\{\}$ braces are evaluated at $r_{i+1/2}$ using an arithmetic average.

Finally, the overall flow of an integration step is as follows:

- (a) Begin with the data for time $t = t^n$: $\{\Pi^n, \Phi^n, P^n, v^n, \alpha^n, a^n\}$.
- (b) Reconstruct the conservative variables using (62) and (63) to obtain values at the cell interfaces for $\{\tilde{q}^\ell, \tilde{q}^r\}$, and calculate the corresponding primitive values, $\{\tilde{w}^\ell, \tilde{w}^r\}$, using (33) and (81). Using the characteristic information in appendix A, calculate the numerical fluxes $F(\tilde{q}^\ell, \tilde{q}^r)$ using (B4) and (B5).
- (c) Begin integrating the equations of motion, (B7), and the momentum constraint, (B8), by perform the predictor step of the modified Euler method (71), obtaining $\{\Pi^*, \Phi^*, a^*\}$, then calculate $\{P^*, v^*\}$ using (33) and (81). Integrate the slicing condition (B9) to determine α^* .
- (d) Reconstruct cells for $\{\tilde{q}^{\ell*}, \tilde{q}^{r*}\}$, and $\{\tilde{w}^{\ell*}, \tilde{w}^{r*}\}$, and calculate the numerical fluxes $F(\tilde{q}^{\ell*}, \tilde{q}^{r*})$.
- (e) Perform the corrector step of the modified Euler method (72), obtaining $\{\Pi^{n+1}, \Phi^{n+1}, a^{n+1}\}$, then calculate $\{P^{n+1}, v^{n+1}\}$, and integrate the slicing condition to determine α^{n+1} .
- (f) Check the regridding criteria and regrid if necessary.

Appendix C. Additional tests

This section describes some code tests which fall outside the main development, including: tests of the shock-capturing algorithm with Riemann shock-tube solutions, an independent residual test of the evolution equation for τ and a test of the sensitivity of the $\Gamma = 2$ critical solutions to the magnitude of the floor.

The Riemann problem is an exact solution for two initial constant states separated by a divider at $t = 0$

$$\mathbf{q}(x, 0) = \begin{cases} \mathbf{q}_\ell & \text{if } x < x_0 \\ \mathbf{q}_r & \text{if } x > x_0. \end{cases} \quad (\text{C1})$$

This solution can be used to test the shock-capturing algorithm, checking that the code calculates the shock jumps and velocities correctly. Two shock-tube PDE solutions plotted together with the analytic solutions are shown in figures C1 and C2.

While the shock tube provides a good test of the fluid solver, the calculation is done in Minkowski space with slab symmetry, and thus can probe neither the implementation of the geometric factors in the fluid equations, nor the discretized Einstein equations. A few general relativistic fluid systems *can* be solved exactly, and have traditionally been used to test new

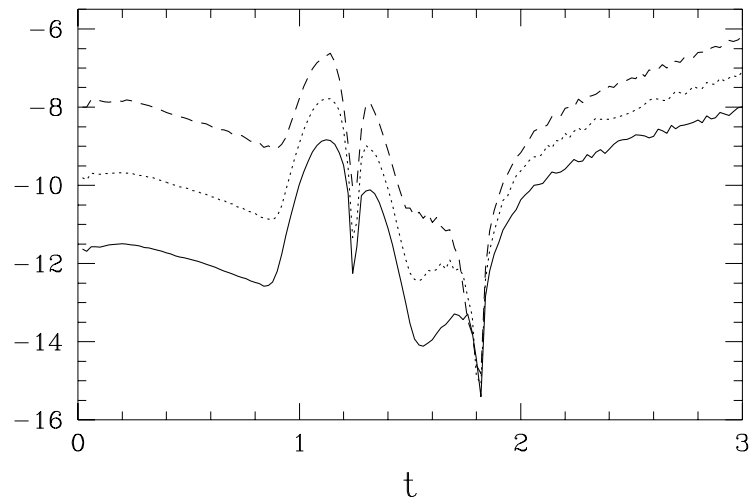


Figure C1. The shock compression of a diffuse relativistic gas is demonstrated in this shock-tube test of a $\Gamma = \frac{4}{3}$ fluid. This shock-tube test is equivalent to the fluid hitting a wall at $x = 0.5$. The full lines show the exact solution, and the points correspond to the PDE solution. The top frame shows the pressure at $t = 0.6$, and the bottom frame shows the product of the Lorentz factor and the velocity. The initial left state is $P_\ell = 10^{-4}$, $v_\ell = 0.9999995$, and the initial right state is $P_r = 10^{-4}$, $v_r = -0.9999995$. The solution is calculated with 400 cells.

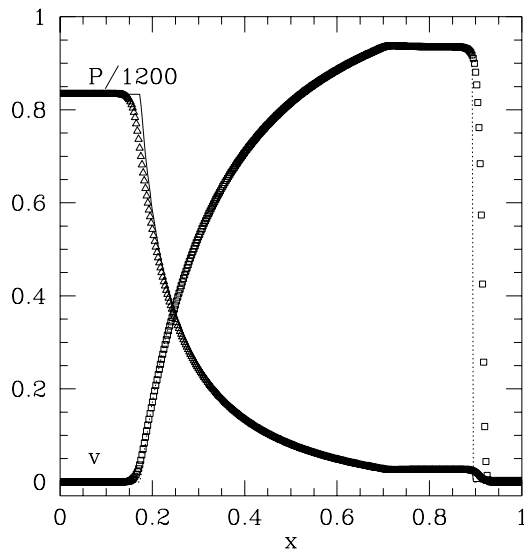


Figure C2. The curves show the exact solution for this shock-tube test with a $\Gamma = \frac{5}{3}$ fluid at $t = 0.4$. The triangles and squares show the pressure and velocity of the PDE solution, respectively. The initial left state is $P_\ell = 10^3$, $v_\ell = 0$, and the initial right state is $P_r = 1$, $v_r = 0$. The solution is calculated with 400 cells.

codes, including static, spherical stars (Tolman–Oppenheimer–Volkoff, TOV) and spherical dust collapse (Oppenheimer–Synder). The TOV solutions for the ultrarelativistic EOS have the form $\rho \propto 1/r^2$ [41]; our code, however, requires regularity at the origin, precluding this as a possible test.

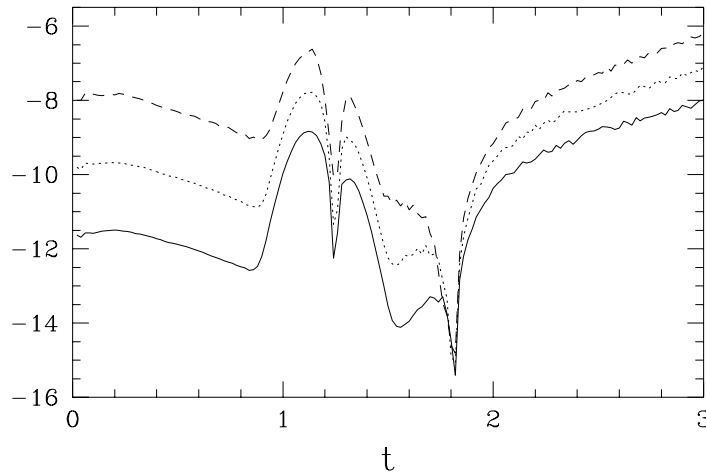


Figure C3. A plot of $\ln \|T^h\|_2 / \ln \|\tau^h\|_2$ as a function of time for three different resolutions, where T^h is the residual of the τ equation of motion (24), and $\|\cdot\|_2$ is the ℓ_2 norm. The initial data describes a time symmetric fluid shell with a Gaussian profile and $\Gamma = 2$. Part of the fluid collapses, reaching its maximum compression at $t \approx 1.82$, and then the fluid disperses from the origin. The evolutions were performed on a uniform grid with spacings $\Delta r = h$ (full curve), $\Delta r = 2h$ (dotted), and $\Delta r = 4h$ (broken). Initially, the curves differ by 2 on the vertical scale, indicating that the residual converges quadratically to zero. When the bulk of the fluid reaches the origin, the convergence decreases, indicating that the largest errors occur at the origin.

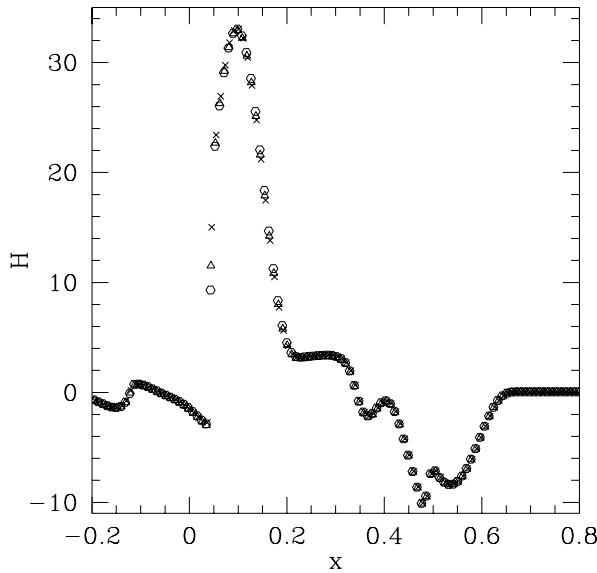


Figure C4. The residual of the Hamiltonian constraint, H , for a $\Gamma = 2$ sub-critical solution calculated with three different floors at the same resolution. The crosses show the residual for $\delta = 10^{-6}$, the triangles for $\delta = 10^{-8}$ and the circles for $\delta = 10^{-10}$. The residuals provide an independent check of the truncation error, and are directly a function of the resolution used to calculate the solution. As illustrated in this figure, the residuals are not a function of the floor, indicating that the magnitude of the floor does not strongly affect the solution. However, the mere presence of a non-zero floor may affect the solution.

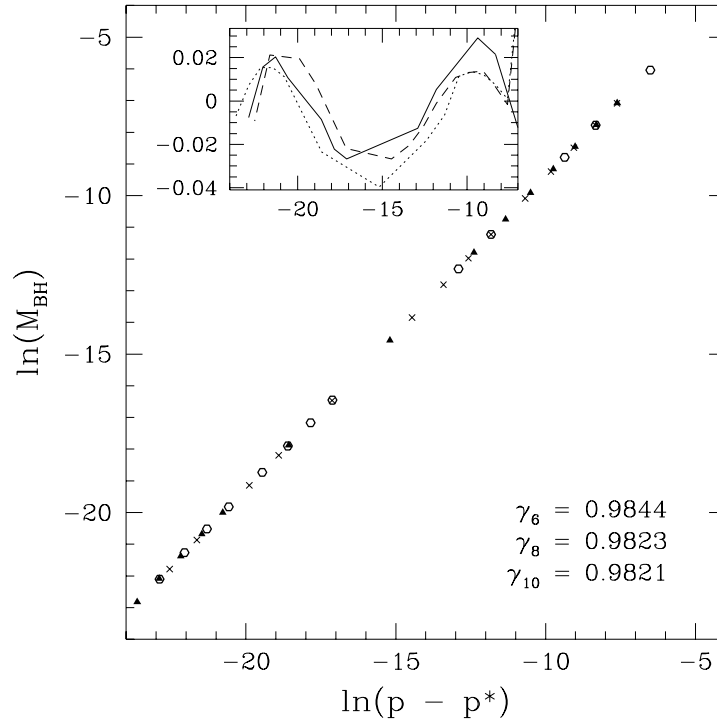


Figure C5. The black-hole mass as a function of critical parameter for $\Gamma = 2$ super-critical evolutions with three different floors with the same resolution. The crosses show the black-hole masses calculated when $\delta = 10^{-6}$, the triangles when $\delta = 10^{-8}$ and the circles when $\delta = 10^{-10}$. The black-hole mass is a simple function of the critical parameter [12], and this figure shows that the floor does not strongly affect measurements of the mass-scaling parameter from super-critical evolutions. In the lower right-hand corner, we show the mass-scaling coefficients obtained from a least-squares fit of the data, the subscript on γ indicating the floor. (Note that these coefficients are indicative only of the insensitivity to the floor. More accurate measurements of γ for $\Gamma = 2$ are made in [12] with higher-resolution solutions.) The inset in the upper left-hand corner shows the deviation of the data points from the least squares fit. The full curve when $\delta = 10^{-10}$ the dotted curve when $\delta = 10^{-8}$, and the broken curve when $\delta = 10^{-6}$. Again this deviation shows no dependence on the floor magnitude.

The independent residual test can be used to verify that the discretized equations solved by our Einstein/fluid code correspond to the correct continuum equations. In this test we discretize the PDEs using the leap-frog scheme, writing the equations such that the ‘right-hand side’ is zero, and evaluate these leap-frog equations with the solution calculated by our Einstein/fluid code. The ‘left-hand side’ is the *residual*, which is generically non-zero. Using a uniform grid and a sub-critical $\Gamma = 2$ fluid, we performed residual tests using the evolution equations for τ and S (24), and the Hamiltonian constraint (19). Figure C3 shows the ℓ_2 norm of the residual of the τ equation at three resolutions as a function of time. Although not explicitly shown here, the residuals for the S equation of motion and the Hamiltonian constraint display completely analogous behaviour. Taken together, these residual tests clearly indicate that our discrete critical solutions are converging to continuum solutions of the PDEs.

Finally, to test the sensitivity of the critical solutions to the *magnitude* of the floor, δ , we constructed near-critical solutions for $\Gamma = 2$ using $\delta = 10^{-6}$, $\delta = 10^{-8}$ and $\delta = 10^{-10}$ with the same spatial resolution. The residuals of the Hamiltonian constraint (19) for these three

solutions are essentially identical, as shown in figure C4. We also measured the mass-scaling exponent for the $\Gamma = 2$ fluid using the three floor values by evolving super-critical initial data, and again find no dependence on the floor magnitude (see figure C5).

References

- [1] Choptuik M W 1993 *Phys. Rev. Lett.* **70** 9
- [2] Gundlach C 1998 *Adv. Theor. Math. Phys.* **2** 1
(Gundlach C 1997 *Preprint* gr-qc/9712084)
- [3] Evans C R and Coleman J S 1994 *Phys. Rev. Lett.* **72** 1782
- [4] Koike T, Hara T and Adachi S 1995 *Phys. Rev. Lett.* **74** 5170
- [5] Maison D 1996 *Phys. Lett. B* **366** 82
- [6] Hara T, Koike T and Adachi S 1996 *Preprint* gr-qc/9607010
- [7] Koike T, Hara T and Adachi S 1999 *Phys. Rev. D* **59** 104008
- [8] Brady P R and Cai M J 1998 *Preprint* gr-qc/9812071
- [9] Goliath M, Nilsson U S and Uggla C 1998 *Class. Quantum Grav.* **15** 2841
- [10] Carr B J, Coley A A, Goliath M, Nilsson U S and Uggla C 1999 *Preprint* gr-qc/990131
- [11] Carr B J, Coley A A, Goliath M, Nilsson U S and Uggla C 1999 *Preprint* gr-qc/990270
- [12] Neilsen D W and Choptuik M W 2000 *Class. Quantum Grav.* **17** 761
(Neilsen D W and Choptuik M W 1998 *Preprint* gr-qc/9812053)
- [13] Cahill M E and Taub A H 1971 *Commun. Math. Phys.* **21** 1
- [14] Ori A and Piran T 1990 *Phys. Rev. D* **42** 1068
- [15] Evans C R 1993 *Lecture Notes of the Numerical Relativity Conf., Penn State University 1993* unpublished
- [16] Norman M L and Winkler K-H A (ed) 1986 *Astrophysical Radiation Hydrodynamics* (Dordrecht: Reidel) p 449
- [17] Godunov S K 1959 *Mat. Sb.* **47** 271
- [18] LeVeque R J 1992 *Numerical Methods for Conservation Laws* (Basel: Birkhäuser)
- [19] LeVeque R J 1998 *Computational Methods for Astrophysical Fluid Flow (27th Saas-Fee Advanced Course Lecture Notes)* (Berlin: Springer) to be published, also available at <ftp://amath.washington.edu/pub/tjl/papers/saasfee.ps.gz>
- [20] Ibáñez J Ma and Martí J Ma 1999 *J. Comput. Appl. Math.* **109** 173
- [21] Smoller J and Temple B 1993 *Commun. Math. Phys.* **156** 67
- [22] Martí J Ma and Müller E 1994 *J. Fluid Mech.* **258** 317
- [23] Balsara D S 1994 *J. Chem. Phys.* **114** 284
- [24] Dai W and Woodward P R 1997 *SIAM J. Sci. Comput.* **18** 982
- [25] Schneider V, Katscher U, Rischke D H, Waldhauser B, Maruhn J A and Munz C-D 1993 *J. Chem. Phys.* **105** 92
- [26] van Leer B 1979 *J. Comput. Phys.* **32** 101
- [27] Roe P L 1981 *J. Comput. Phys.* **43** 357
- [28] Ibáñez J Ma, Martí J Ma, Miralles J A and Romero J V 1992 *Approaches to Numerical Relativity* (Cambridge: Cambridge University Press) p 223
- [29] Eulderink F and Mellema G 1995 *Astron. Astrophys. Suppl.* **110** 587
- [30] Romero J V, Ibáñez J Ma, Martí J Ma and Miralles J A 1996 *Astrophys. J.* **462** 839
- [31] Banyuls F, Font J A, Ibáñez J Ma, Martí J Ma and Miralles J A 1997 *Astrophys. J.* **476** 221
- [32] Brandt S, Font J A, Ibáñez J Ma, Massó J and Seidel E 1998 *Preprint* gr-qc/9807017
- [33] Font J A, Miller M, Suen W and Tobias M 1998 *Preprint* gr-qc/9811015
- [34] Quirk J J 1994 *Int. J. Numer. Methods Fluids* **18** 555
- [35] Donat R and Marquina A 1996 *J. Comput. Phys.* **125** 42
- [36] Donat R, Font J A, Ibáñez J Ma and Marquina A 1998 *J. Chem. Phys.* **146** 58
- [37] Thornburg J 1999 *Preprint* gr-qc/9906022
- [38] Shu C-W and Osher S 1988 *J. Comput. Phys.* **77** 439
- [39] Berger M J and Olinger J 1984 *J. Comput. Phys.* **53** 484
- [40] Garfinkle D 1995 *Phys. Rev. D* **51** 5558
- [41] Schutz B F 1990 *A First Course in General Relativity* (Cambridge: Cambridge University Press)